Current-error space-vector-based hysteresis PWM controller for three-level voltage source inverter fed drives

P.N. Tekwani, R.S. Kanchan and K. Gopakumar

Abstract: A current-error space-vector-based PWM hysteresis controller is proposed for three-level voltage source inverter fed induction motor drive applications. A hexagonal boundary for the current-error space vector is formed by sensing the current-error space vector along three different axes, which are 120° apart and are orthogonal to machine phase axes. Only the adjacent inverter voltage vectors forming a triangular sector, in which tip of the machine voltage vector lies, are switched to keep the current-error space vector within the hexagonal boundary. Selection amongst the three nearest voltage vectors is done by a simple region detection logic in all the sectors. Calculation of the machine voltage vector is not needed and information of the same is indirectly derived from the direction of current-error space vector. The controller uses a self-adaptive sector identification logic, which provides smooth transition between sectors (voltage levels), including over modulation region up to 12-step mode of operation. Inherent advantages of current hysteresis controller are retained with the added advantage of adjacent voltage vector selection for hysteresis PWM control. Simple look-up tables are only needed for sector and vector selection, based on the hysteresis controller output, for the proposed hysteresis PWM controller. Experimental verification is provided by implementing the proposed controller on a 1.5 kW open-end winding induction motor drive. The proposed controller can be extended for further levels of multi-level inverters for high-performance drives by constructing suitable look-up tables.

1 Introduction

Current-controlled PWM (CC-PWM) inverters offer considerable advantages as compared to conventional voltage-controlled PWM voltage source inverters (VSIs) [1, 2], and hence are extensively employed in high-performance-drive (HPD) systems. Different ways of classification of current controllers can be found in [1–3], amongst which the hysteresis controllers are widely used because of their inherent simplicity and fast dynamic response [1, 3–5]. However, some of the drawbacks of conventional type of hysteresis controller, e.g. limit cycle oscillations, overshoot in current error, generation of sub-harmonic components in the current and random (non-optimum) switching [2–4, 6] are very well known. Current-error space-vector-based hysteresis controllers [4–9] allow the current-error space vector to move within a specified boundary. Hexagonal, circular and rectangular shapes of current-error space-vector boundary are reported in the literature [1, 2, 4–9]. Attempts have been made to minimise the overshoot in current error, limit cycle oscillations [4], inverter switching frequency [5, 10, 11] and to achieve fast transient response [7, 12]. The multi-level comparator-based scheme discussed in [13] ensures the optimum switching only in the steady state. In [2] and [14], space-vector-based hysteresis controllers with adaptive switching pattern schemes are proposed, to reduce the inverter switchings and the number of double commutation. The space-vector-based hysteresis controllers presented in [8] and [15] ensure adjacent voltage vector selection for PWM current control of two-level VSIs.

In the field of hysteresis controllers, until now most of the research has been concentrated on getting the optimum switching and fast dynamic response in association with inherent advantages of hysteresis current controller for two-level VSIs. Extension of these strategies to multi-level VSIs is much less established. For high-power drive applications, multi-level inverters have become the preferred solution because of significant inherent advantages offered by them. Recently, [9, 16–18] have focused on the hysteresis type current controllers for multi-level drives. A time-based current regulator [16] and improved time-based double-band hysteresis controller [17] are presented, based on recursive selection of inverter switch states using a logic state machine. However, these are proposed for single-phase multilevel inverters and adjacent voltage vector switching is not guaranteed during transients [16, 17]. A space vector based current control for three-level inverter with adjacent voltage vector selection is presented in [9], where the concept is supported only by simulation results, and experimental verifications are not provided. In [18], a four-level hysteresis PWM control is suggested in which optimum switching during level transitions and speed reversal issues have not been discussed. Also, the switching state diagram is implemented in [18] using several operational amplifiers for each phase and improper selection of the integral gain of synchronous current regulator significantly affects the system dynamics.

IEE Proceedings online no. 20050109

doi:10.1049/ip-epa:20050109

Paper first received 5th November 2004 and in final revised form 4th May 2005

The authors are with the Centre for Electronic Design and Technology, Indian Institute of Science, Bangalore 560 012, India

E-mail: kgopa@cedt.iisc.ernet.in

In this paper, a current-error space-vector-based hysteresis controller is presented, for three-level VSI fed induction motor drives. It does not need computation of machine back EMF space vector for sector identification and information on the same is indirectly derived from the directions of current-error space vector. The inverter voltage vector (among the three adjacent vectors forming a triangular sector, in which the tip of the machine voltage vector lies), which will result in the largest current error deviation away from the proposed hexagonal boundary, is selected throughout the operating range based on the output of hysteresis comparators. This ensures the optimum PWM vector selection and fast dynamic response of the controller. The scheme is self-adaptive for any possible amplitude and position of the machine voltage vector. The proposed scheme is implemented on a dual two-level voltage source inverter fed open-end winding induction motor drive [9, 19, 20]. The technique is theoretically explained, and experimentally verified on a 1.5 kW open-end winding induction motor using field-oriented control.

2 Three-level voltage space-vector generation and current-error space-vector detection

The present control scheme can be used for any inverter configuration that provides three-level voltage space vector structure. A dual two-level inverter fed open-end winding induction motor configuration, shown in Fig. 1*a*, which provides a three-level inverter voltage space vector structure, is used in the present work [19, 20]. The DC-link voltage requirement of each two-level inverter in Fig. 1*a* is $V_{dc}/2$ as compared to V_{dc} for a conventional three-level NPC VSI. Both the two-level inverters of Fig. 1*a* (inverter I and inverter II) are supplied with isolated DC-links to eliminate the flow of zero sequence current in the machine phases [19, 20]. A dual two-level inverter fed open-end winding induction motor drive with common-mode voltage elimination, presented in [21], uses the common DC-link for both the two-level inverters. However, with the elimination of common-mode voltage, the scheme presented in [21] is capable of generating only a two-level voltage space vector

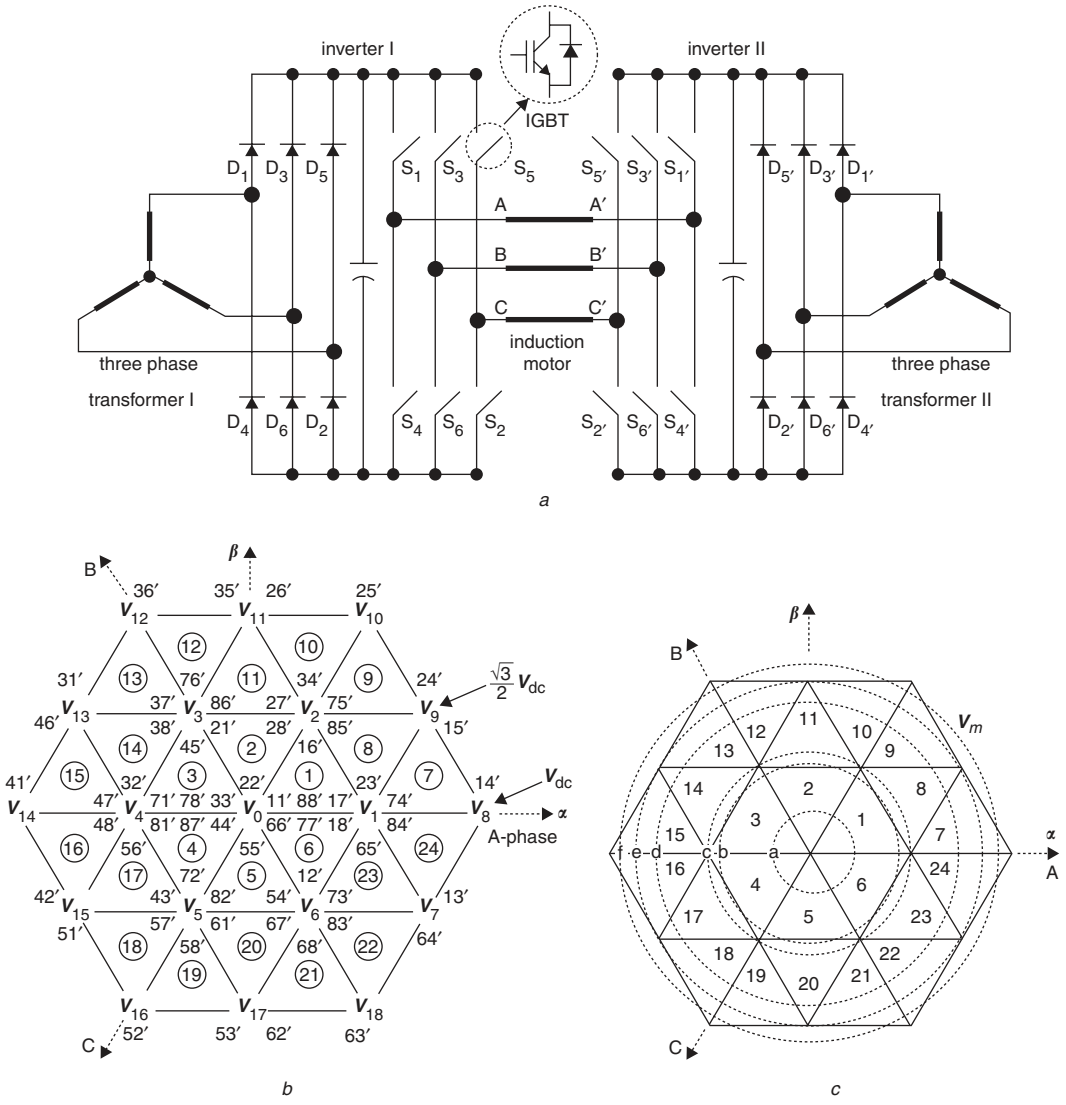

Fig. 1
a Power schematic of a dual two-level inverter fed open-end windings induction motor drive resulting in three-level inverter voltage space vector structure
b Resultant three-level inverter voltage space vector structure showing combined voltage space vector locations with corresponding switching state combinations
c Various possible trajectories of rotation of V_m with respect to the three-level inverter voltage space vector locations (numbers 1 to 24 indicate the triangular sectors formed by the inverter voltage vectors)

structure. But in the proposed scheme the three-level inverter voltage space vector structure is realised (Fig. 1*b*) by using two isolated DC-links. When both the two-level inverters of Fig. 1*a* are switched independently, the overall configuration of Fig. 1*a* results in a total of 64 switching state combinations (compared to the 27 for a conventional three-level NPC VSI [20]), which generate a total of 19 combined voltage vectors $\boldsymbol{V_0}-\boldsymbol{V_{18}}$, as shown in Fig. 1*b*. Three combined voltage vectors form a triangular sector, and 24 such triangular sectors are shown in Fig. 1*b*.

The current error space vector $\boldsymbol{\Delta i}$ for the inverter of Fig. 1*a* is derived as a vectorial difference of machine current space vector $\boldsymbol{i}$ and reference current space vector $\boldsymbol{i}^*$, as given in (1) [8]. The relation between the inverter voltage vector $\boldsymbol{V_k}$ (k can be any number from 0 to 18), rate of change of current-error space vector $d\boldsymbol{\Delta i}/dt$, and the machine voltage vector $\boldsymbol{V_m}$ can be represented by (2), where L_σ is the stator leakage inductance of the machine [8, 9, 13]:

$$\boldsymbol{\Delta i} = \boldsymbol{i} - \boldsymbol{i}^* \tag{1}$$

$$\frac{d\boldsymbol{\Delta i}}{dt} = \frac{\boldsymbol{V_k} - \boldsymbol{V_m}}{L_\sigma} \tag{2}$$

Figure 1*c* shows the various trajectories along which the tip of $\boldsymbol{V_m}$ can move for all possible combinations of the sector change. These trajectories indicate different-modes of operation of inverter e.g. '*a*' indicates two-level, '*d*' indicates three-level, and '*f*' indicates the over-modulation operation of the drive.

3 Analysis of proposed current-error space-vector based hysteresis PWM controller

For proper functioning of the controller, identification of the direction and amplitude of the current-error space vector and identification of sector (in which the tip of $\boldsymbol{V_m}$ lies) are achieved by using the hysteresis controller outputs and simple look-up tables, as discussed in the following Subsections.

3.1 Formation of boundary for current-error space vector

The positions of $\boldsymbol{V_m}$ in two different sectors (sector 7 and sector 8) are shown in Fig. 2*a*. For the position of $\boldsymbol{V_m}$ in the direction **OP** ($\boldsymbol{V_{m1}}$) in sector 7, directions of the current error space vector corresponding to the switching of inverter

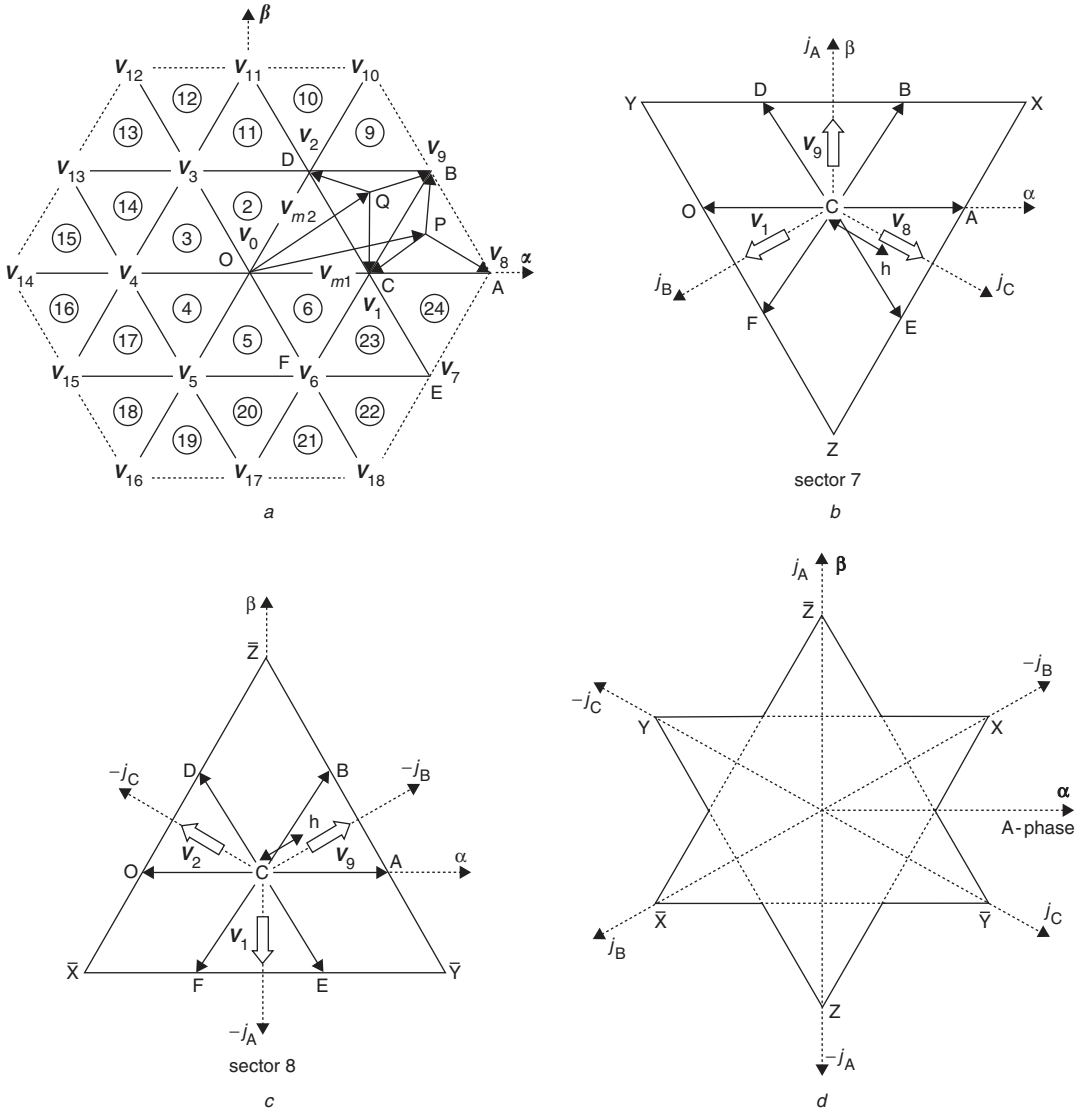

Fig. 2
a Directions of current error space vector for position of $\boldsymbol{V_m}$ in sector 7 and sector 8
b Boundary for current error space vector for $\boldsymbol{V_m}$ in sector 7
c Boundary for current error space vector for $\boldsymbol{V_m}$ in sector 8
d Combined boundary for current error space vector

voltage vectors V_8, V_9, and V_1 can be determined based on (2) and are along **PA**, **PB**, and **PC**, respectively, as shown in Fig. 2*a*. Based on position and amplitude of V_m, these directions of movement of current-error space vector can change for the same sector and for the same inverter voltage vectors.

For the direction of V_{m1} along **OA** with its tip lying anywhere on **CA**, switching of V_8 will have current error space vector direction along **CA**. When V_{m1} has its tip on point **B**, and if V_8 is switched, then the current error space vector will have its direction along **BA** (parallel to **CE**). Hence, for any position of V_{m1} in sector 7, for the switching of V_8 the current-error space vector direction is confined between a set of two directions **CA** and **CE**. Similar sets of directions confining the current-error space vector movement can be found for switching of V_9 and V_1 for any position of V_{m1} in sector 7. Intersection of the boundaries formed by these three sets of directions lead to a triangular boundary XYZ for current error space vector when V_m is in sector 7, as shown in Fig. 2*b* (thick arrows point to the sides of the triangular boundary towards which the current-error space vector moves when particular voltage vector is switched, e.g. XZ boundary corresponds to the direction of current-error space vector due to switching of V_8). The current error limits (hysteresis or tolerance bands) are set at distance 'h' on to the three axes j_A, j_B and j_C, which are 120° apart and orthogonal to the machine phase axes A, B and C [8, 9]. In a similar way, it is verified that the triangular boundary XYZ exists for all the odd-numbered sectors and the triangular boundary $\bar{X}\bar{Y}\bar{Z}$ (as shown in Fig. 2*c*) exists for all the even-numbered sectors [8]. The combined boundary for current-error space vector when V_m moves through all the sectors is shown in Fig. 2*d*.

3.2 Selection of inverter voltage vector for each sector

Since, only the three switching voltage vectors of the inverter are involved in a sector, it is proposed to divide the triangular boundaries into three different regions. Figure 3*a* shows the regions R_1, R_2, and R_3 of the triangular boundary for any odd sector and $\bar{R}_1$, $\bar{R}_2$ and $\bar{R}_3$ for any even numbered sector. In the proposed strategy, the same inverter voltage vector is supplied continuously until the error space vector touches the boundary. Once the current-error space vector touches the boundary, another appropriate inverter voltage vector is switched to keep the current-error space vector within the boundary. Figure 3*b* shows the uniquely associated inverter voltage vectors to be switched when current-error space vector touches the different regions of triangular boundary for position of V_m in sector 7 and sector 8. As an example, for V_m in sector 7, the voltage vectors V_1, V_8 and V_9 are to be switched, respectively, for the regions R_1, R_2, and R_3. In a similar way, the appropriate inverter voltage vectors to be switched for different regions for positions of V_m in different sectors are found and are given in Table 1.

For the combined boundary of Fig. 2*d*, the error space vector may move to double the distance, along the $-j_A$, $-j_B$, and $-j_C$ axes in the case of odd sectors and along the j_A, j_B and j_C axes for the even sectors. Hence, a boundary limit is suggested along all the six directions j_A, j_B, j_C, $-j_A$, $-j_B$ and $-j_C$, leading to a resultant hexagonal boundary for current-error space vector, as shown in Fig. 3*c*. Figure 3*d* shows modified regions of the hexagonal boundary for the odd and even sectors. However, inverter voltage vectors to be switched for different regions for various sectors remain the same (Table 1) with these modified shapes of the regions.

The redundancy (multiplicity) in switching state combinations (Fig. 1*b*) is utilised for reducing the inverter switchings, while switching the particular voltage vector for PWM current control. One of the inverters is kept clamped at a particular switching state and the other inverter is switched in a sector to realise the commanded voltage vectors. For the next adjacent sector the other inverter is kept clamped and the first one is switched. This ensures that inverter I and inverter II (Fig. 1*a*) are switched equally over a fundamental period of reference current. Table 2 gives the switching state combinations selected for realising the voltage vectors of Table 1.

3.3 Region detection on hexagonal boundary

Identification of the unique region is achieved by hysteresis current error comparators along the directions perpendicular to the sides of the hexagonal boundary (i.e. along the directions j_A, j_B, j_C, $-j_A$, $-j_B$ and $-j_C$) [8, 9], as shown by the inner comparators in Fig. 3*e*. For an example, the current error Δi_{j_A} along the j_A axis is defined as in (3), where $i^*_{j_A}$ is the component of the reference current space vector along the j_A axis and the machine current component along the j_A axis is computed as in (4):

$$\Delta i_{j_A} = i_{j_A} - i^*_{j_A} \tag{3}$$

$$i_{j_A} = \frac{\sqrt{3}}{2}(i_B - i_C) \tag{4}$$

The inner comparator remains in OFF state when current error space vector is within the hysteresis band along that particular direction. When the current error space vector touches the hysteresis band along that particular axis, the comparator switches to the ON state. As shown in Fig. 3*f*, each side of the hexagonal boundary is divided into two segments. The segment at which the current error space vector touches the hexagonal boundary is identified by a simple logic. For example, consider the tip of V_m in sector 7. Now

when the state of comparator along $j_A = 1$;

and; if $\Delta i_{j_B} \geq \Delta i_{j_C} \Rightarrow$ segment detected is R_{a1} (Fig. 3*f*);

;else $\Rightarrow$ segment detected is R_{a2}

Based on the segment information, regions on the hexagonal boundary are uniquely identified from Fig. 3*f*, e.g. if segment detected is R_{a2} or $\bar{R}_{b1}$ or $\bar{R}_{b2}$ or R_{c1}, region identified is R_1.

High-frequency switching between two voltage vectors of the inverter can occur when the current-error space vector touches the hexagonal boundary exactly along any of the sensing directions (i.e. j_A, j_B, j_C, $-j_A$, $-j_B$ or $-j_C$). This gets reflected as a 'jitter' in the inverter output voltage. The proposed controller avoids this phenomenon. Once a voltage vector is selected, the controller applies a new voltage vector only if the current-error space vector comes within the hexagonal boundary and touches the boundary at some other region (i.e. when some other comparator comes into the ON state); until then the previously switched voltage vector is continued to avoid the 'jitter'.

3.4 Self-adaptive sector selection logic

A self-adaptive logic is used in the proposed controller to identify the instants at which the V_m crosses from one sector to another. This sector change is identified with the help of another set of comparators (outer comparators) placed a little further away from the inner comparators, as shown in

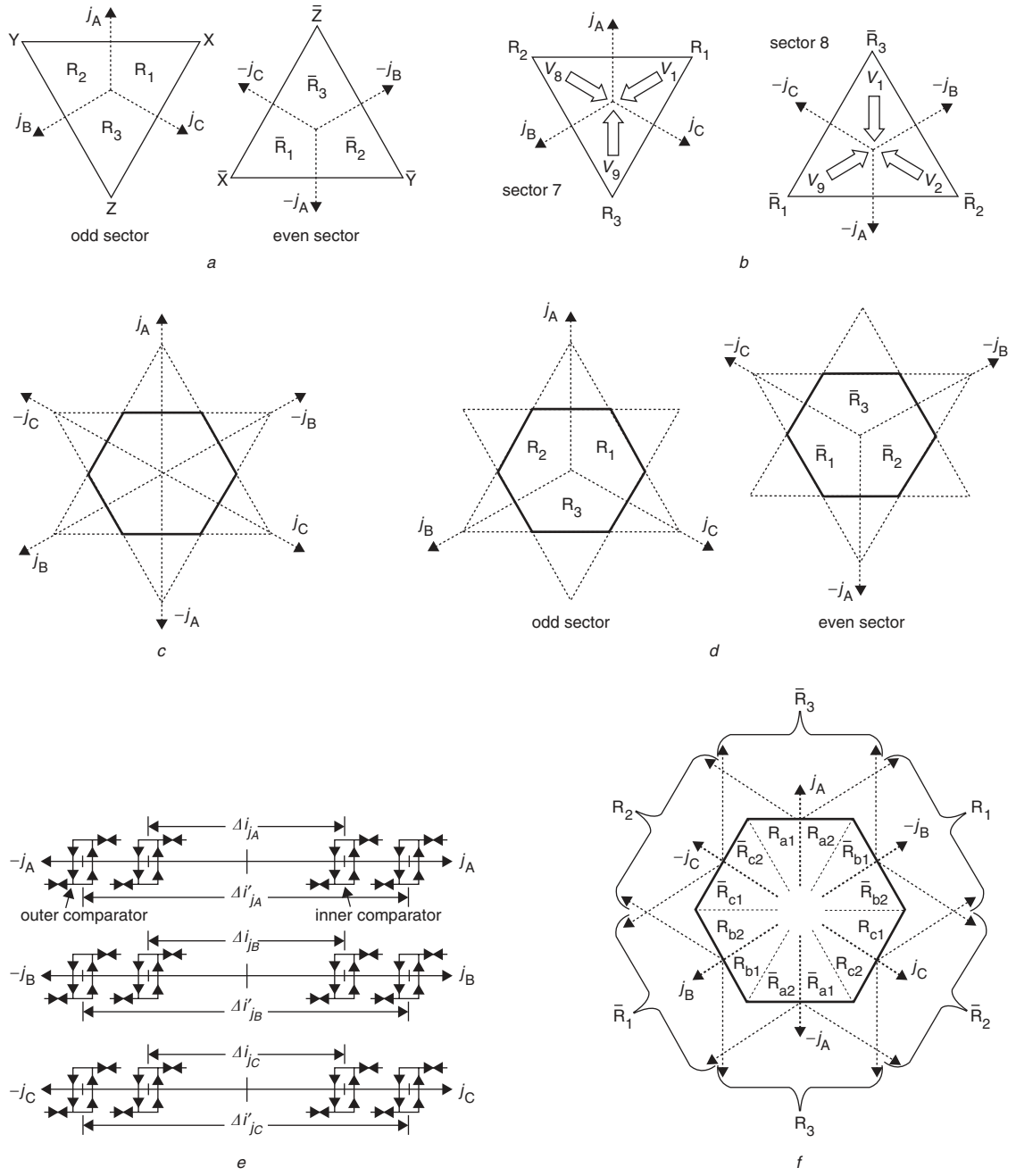

Fig. 3
a Regions of current-error space vector boundary for odd and even sectors
b Voltage vectors to be switched for corresponding regions when V_m in sector 7 and sector 8
c Hexagonal boundary for current-error space vector
d Regions of hexagonal boundary for odd sector and even sector
e Inner comparators for region detection and outer comparators for detecting the sector change
f Region formation from segments of hexagonal boundary

Fig. 3*e* [8]. All the trajectories of V_m (Fig. 1*c*) are considered for the analysis of possible sets of sector changeovers, during different modes of operation of inverter.

3.4.1 Sector change along trajectory 'a', 'b', and 'd': In the proposed scheme, the anticlockwise movement of V_m is considered as the forward direction of rotation of the machine. Along the trajectory '*d*', let V_m move from sector 7 to sector 8. When V_m is very close to the boundary of sector 7 and sector 8, the controller will select either V_9 or V_1 as these are near to V_m. When V_m has its tip anywhere on **CB** (boundary of sector 7 and sector 8, Fig. 2*a*), and either of the vectors V_9 or V_1 is switched then, based on (2), the current-error space vector will move along the directions parallel to **CB**. In this case, the rate of change of current-error space vector along the j_C axis will be zero as **CB** is perpendicular to the j_C axis. Now, if the machine voltage vector crosses to sector 8 from sector 7, the deviation of the current-error space vector will increase in the j_C direction and may cross the hexagonal boundary, consequently making the inner comparator along the j_C axis in the ON state. However, the controller is yet to detect the sector change and the controller takes all the action as if the machine voltage vector is in sector 7. Therefore, the region detection logic will identify that the current-error space vector has crossed the segment R_{c2} (region R_3 for sector 7,

Table 1: Region and corresponding combined voltage vector to be switched for various sectors (Figs. 1*b* and 3*b*)

Sector	Region					
	R_1	R_2	R_3	$\bar{R}_1$	$\bar{R}_2$	$\bar{R}_3$
1	V_0	V_1	V_2	–	–	–
2	–	–	–	V_2	V_3	V_0
3	V_4	V_0	V_3	–	–	–
4	–	–	–	V_0	V_4	V_5
5	V_5	V_6	V_0	–	–	–
6	–	–	–	V_1	V_0	V_6
7	V_1	V_8	V_9	–	–	–
8	–	–	–	V_9	V_2	V_1
9	V_2	V_9	V_{10}	–	–	–
10	–	–	–	V_{10}	V_{11}	V_2
11	V_3	V_2	V_{11}	–	–	–
12	–	–	–	V_{11}	V_{12}	V_3
13	V_{13}	V_3	V_{12}	–	–	–
14	–	–	–	V_3	V_{13}	V_4
15	V_{14}	V_4	V_{13}	–	–	–
16	–	–	–	V_4	V_{14}	V_{15}
17	V_{15}	V_5	V_4	–	–	–
18	–	–	–	V_5	V_{15}	V_{16}
19	V_{16}	V_{17}	V_5	–	–	–
20	–	–	–	V_6	V_5	V_{17}
21	V_{17}	V_{18}	V_6	–	–	–
22	–	–	–	V_7	V_6	V_{18}
23	V_6	V_7	V_1	–	–	–
24	–	–	–	V_8	V_1	V_7

Table 2: Switching state combinations selected for realising the voltage vectors of Table 1 for different sectors and regions (Fig. 1*b*)

Sector	Region					
	R_1	R_2	R_3	$\bar{R}_1$	$\bar{R}_2$	$\bar{R}_3$
1	87′	17′	27′	–	–	–
2	–	–	–	85′	86′	88′
3	48′	88′	38′	–	–	–
4	–	–	–	88′	81′	82′
5	57′	67′	77′	–	–	–
6	–	–	–	74′	77′	73′
7	84′	14′	24′	–	–	–
8	–	–	–	15′	16′	17′
9	85′	15′	25′	–	–	–
10	–	–	–	25′	26′	27′
11	86′	16′	26′	–	–	–
12	–	–	–	35′	36′	37′
13	46′	86′	36′	–	–	–
14	–	–	–	45′	46′	47′
15	41′	71′	31′	–	–	–
16	–	–	–	47′	41′	42′
17	42′	72′	32′	–	–	–
18	–	–	–	57′	51′	52′
19	52′	62′	72′	–	–	–
20	–	–	–	68′	61′	62′
21	53′	63′	73′	–	–	–
22	–	–	–	64′	67′	63′
23	54′	64′	74′	–	–	–
24	–	–	–	14′	17′	13′

Fig. 3*f*) or R_{c1} (region R_1 for sector 7, Fig. 3*f*) and hence still the vector selected will be $\boldsymbol{V_9}$ or $\boldsymbol{V_1}$, respectively (Table 1). This will further increase the current error deviation along j_C axis and the outer comparator along the j_C axis will also switch to the ON state. Now, based on the state of the outer comparator, the sector changing logic updates the current sector as sector 8. Consequently, the region detection logic will identify that the current error has crossed the hexagonal boundary at region $\bar{R}_2$ (Fig. 3*f*) and for the newly detected sector, i.e. for sector 8, controller will select $\boldsymbol{V_2}$ (Table 1), which will bring back the current-error space vector inside the hexagonal boundary. Therefore, the crossing over of $\boldsymbol{V_m}$ from sector 7 to sector 8 is uniquely identified with the state of the outer comparator along the j_C axis. Similarly, it can also be verified that, if the machine vector moves from the sector 8 to sector 7 (i.e. the motor rotates in the reverse direction) the current error will increase through the $-j_C$ axis.

It is found that, for all the possible sector changeovers along trajectory '*a*', '*b*' and '*d*' whenever the $\boldsymbol{V_m}$ crosses from one sector to the another sector, the current error will increase along a unique axis, which is the axis perpendicular to the boundary of the sectors involved. Based on this, sector changeovers detected along the same direction can be grouped together. Six such sets of sector changeovers (along the j_A, j_B, j_C, $-j_A$, $-j_B$ and $-j_C$ directions) are formed for the counter-clockwise rotation of $\boldsymbol{V_m}$. A set of six sector changeovers which can be detected through the outer comparators placed along the j_A direction is shown in Fig. 4*a*. In a similar way changeovers for other sectors can also be shown.

3.4.2 Sector change along trajectory 'c' (corner to corner sectors): Trajectory '*c*' of the machine voltage vector (Fig. 1*c*) shows that $\boldsymbol{V_m}$ moves across six sectors 8, 11, 14, 17, 20 and 23, which are referred to here as corner sectors. As shown in Fig. 4*b*, when tip of $\boldsymbol{V_m}$ is in sector 23 and approaching point A, $\boldsymbol{V_1}$ will be switched. Consider that the machine voltage vector has crossed the sector and is now in sector 8. But the controller will continue to switch voltage vector $\boldsymbol{V_1}$. Now, in a similar way to the discussion in Subsection 3.4.1, the controller detects sector changeover from sector 23 to sector 8 through the outer comparator along $-j_A$ direction and takes further action by switching the appropriate vectors for the newly detected sector. It will take some time for current error to come inside the outer hysteresis band set on the $-j_A$ axis. Until then the outer comparator along the $-j_A$ direction will remain in the ON state. So, at this instant of time the current sector is sector 8 and the outer comparator on the $-j_A$ axis is ON. Note that, based on the discussion of the previous Subsection, this can be found out to be the condition for the changeover from sector 8 to sector 9. Therefore, if proper logic is not used, sector changeover logic will immediately update the current sector as sector 9, even though $\boldsymbol{V_m}$ is actually in sector 8. This false sector change detection can result in switching of the improper voltage vectors. A similar situation can occur at every transition from a corner sector to another corner sector. This condition is prevented by providing a delay in invoking the sector change logic after detection of every sector

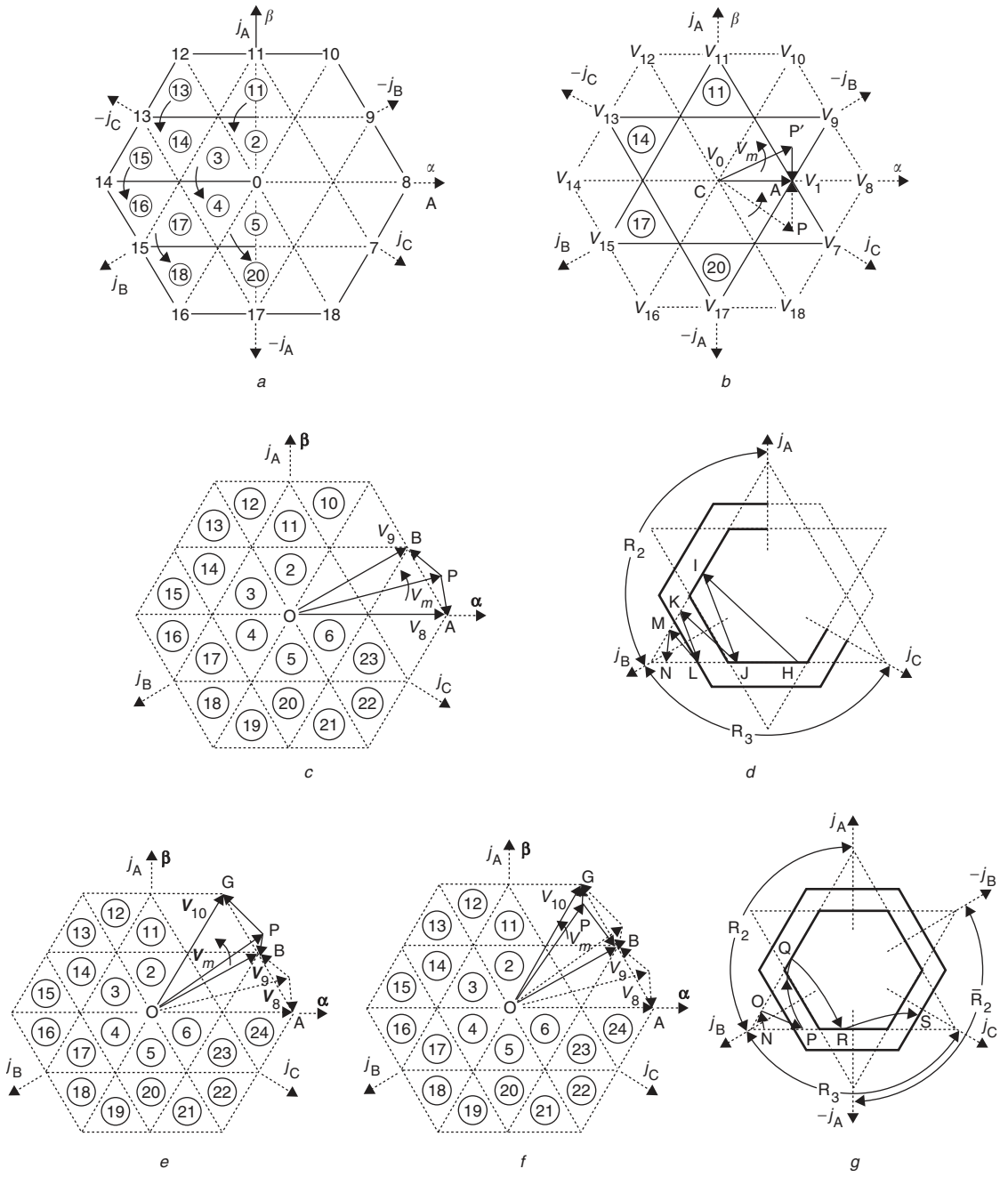

Fig. 4
a Sets of sector changeovers that can be detected by outer hysteresis comparator along j_A direction for counter clockwise rotation of $\boldsymbol{V_m}$
b Current-error space vector during changeover from sector 23 to sector 8
c Directions of current-error space vector during over modulation when $\boldsymbol{V_m}$ is outside sector 7
d Trajectory of current-error space vector during over modulation when $\boldsymbol{V_m}$ crossing from sector 7 to sector 9
e Directions of current-error space vector during over modulation when $\boldsymbol{V_m}$ is outside the sector 9
f Directions of current-error space vector during over modulation when $\boldsymbol{V_m}$ in sector 9
g Trajectory of current-error space vector during over modulation when $\boldsymbol{V_m}$ crossing from sector 9 to sector 10

change. In the proposed scheme, a delay of 200 μs is provided before again inhibiting the sector change once a sector change is effected.

3.4.3 Operation during over-modulation: If demanded by the load, or to take care of voltage variations in the DC-link, the proposed controller is able to operate the drive in the over-modulation region by retaining the feature of adjacent voltage vector switching. Sector change-over during over-modulation is also detected by the outer hysteresis comparators (Fig. 3*e*). As an example, Fig. 4*c* shows the situation, when $\boldsymbol{V_m}$(**OP**) is outside sector 7, and **PA** and **PB** are the directions parallel to which the current-error space vector moves when vectors $\boldsymbol{V_8}$ and $\boldsymbol{V_9}$ are switched, respectively. Figure 4*d* shows the trajectory of the current-error space vector (HIJKL) when the inverter voltage vectors $\boldsymbol{V_9}$ and $\boldsymbol{V_8}$ are switched alternatively when $\boldsymbol{V_m}$ is moving towards sector 9. At point L the sector change is detected and the current sector is updated to sector 9 and then $\boldsymbol{V_{10}}$ is switched (Fig. 3*a*, Table 1) and the current-error space vector will move along **LM**. By this time, $\boldsymbol{V_m}$ comes very close to sector 9. Figure 4*e* shows the situation where the $\boldsymbol{V_m}$(**OP**), is outside sector 9, and **PB** and **PG** are the directions in which the current-error space vector moves

Table 3: Look-up table for sector selection including over modulation (forward direction)

From	Sector change detection To Direction along which the outer comparator is in ON state					
	j_A	j_B	j_C	$-j_A$	$-j_B$	$-j_C$
1	*	8	2	*	*	*
2	*	*	*	11	3	*
3	4	*	14	*	*	*
4	*	*	*	*	17	5
5	20	6	*	*	*	*
6	*	*	*	1	*	23
7	*	9	8	9	*	*
8	*	*	11	9	1	*
9	*	*	10	*	*	*
10	*	*	12	12	11	*
11	2	*	12	*	14	*
12	*	*	*	*	13	*
13	14	*	15	*	15	*
14	17	*	*	*	15	3
15	16	*	*	*	*	*
16	18	*	*	*	18	17
17	18	4	*	*	*	20
18	*	*	*	*	*	19
19	21	20	*	*	*	21
20	*	23	*	5	*	21
21	*	22	*	*	*	*
22	*	24	*	23	*	24
23	*	24	6	8	*	*
24	*	*	*	7	*	*

* Means continue with current sector

Table 4: Look-up table for sector selection including over modulation (reverse direction)

From	Sector change detection To Direction along which the outer comparator is in ON state					
	j_A	j_B	j_C	$-j_A$	$-j_B$	$-j_C$
1	6	8	*	*	*	*
2	*	*	*	11	*	1
3	*	2	14	*	*	*
4	*	*	*	3	17	*
5	20	*	4	*	*	*
6	*	*	*	*	5	23
7	24	*	*	*	*	*
8	23	*	*	*	1	7
9	8	7	*	*	*	7
10	*	*	*	*	*	9
11	2	10	*	*	*	8
12	*	10	*	10	*	11
13	*	12	*	*	*	*
14	*	11	*	13	*	3
15	*	14	13	13	*	*
16	*	*	*	15	*	*
17	*	4	16	14	*	*
18	*	*	16	17	16	*
19	*	*	18	*	*	*
20	*	*	17	5	19	*
21	19	*	20	*	19	*
22	*	*	*	*	21	*
23	22	*	6	*	20	*
24	22	*	*	*	23	22

* Means continue with current sector

when vectors $\boldsymbol{V_9}$ and $\boldsymbol{V_{10}}$ are switched, respectively. Now the controller will select the voltage vector $\boldsymbol{V_9}$ (point M of Fig. 4*d* comes in region R_2 for sector 9) and current error space vector will follow the trajectory along **MN** (parallel to **PB** (Fig. 4*e*)). Again the controller will select $\boldsymbol{V_{10}}$. Repetitive switching between $\boldsymbol{V_9}$ and $\boldsymbol{V_{10}}$ cause the detection of regions R_3 and R_2 for sector 9. Note that, even though the sector change is detected, the current-error space vector will move in the same direction (in this case, along the j_B axis), because sector 7 and sector 9 are odd sectors and have the same region boundaries (Fig. 3*d*). At the same time the machine voltage vector, which is moving at a very high speed, will come inside sector 9, as shown in Fig. 4*f* (trajectory '*f*' of Fig. 1*c*). Now switching of $\boldsymbol{V_9}$ and $\boldsymbol{V_{10}}$ will cause the current-error space vector to follow the directions parallel to **PB** and **PG** (Fig. 4*f*), respectively. These directions of movement will start pulling the current-error space vector away from the j_B direction towards inside the hexagonal boundary. Gradually the current-error space vector will move along the trajectory shown in Fig. 4*g* (along NOPQRS). At point S (Fig. 4*g*), the controller will detect one more sector change, that is changeover from sector 9 to sector 10. This sector changeover will be detected through the outer comparator along the j_C axis. Finally, if demanded the controller smoothly transits into the 12-step mode of operation, where only one vector will be selected for every 30°.

The sector selection logic, including operation in over-modulation, for forward and reverse directions of rotation of the machine is given in Tables 3 and 4, respectively, which are used by the controller as two look-up tables for properly identifying the sector change.

4 Experimental results

The proposed hysteresis controller has been implemented on a laboratory prototype of a 1.5 kW open-end winding induction motor (motor parameters: 1.5 kW, open-end winding, 400 V, 50 Hz, 1440 rpm, four poles, $R_s = 2.08\,\Omega$, $R_r = 1.9\,\Omega$, $L_s = 0.28$ H, $L_r = 0.28$ H, $M = 0.272$ H) drive fed with dual two-level VSI using vector control. Figure 5*a* shows the block diagram of the proposed hysteresis controller for a three-level induction motor drive. Two Hall-effect current transducers (nominal primary current 25 A, turns ratio 1:1000) are used for sensing the machine currents i_A and i_B. For the speed feedback, a speed encoder supplying 2500 pulses/revolution is used. The complete controller is implemented on the TI TMS320LF2407A DSP controller platform. The sampling time of the current controller is kept as 25 μs. The three-phase reference currents are generated depending on the frequency command and the controller is tested with drive for the entire speed range in the forward and reverse directions.

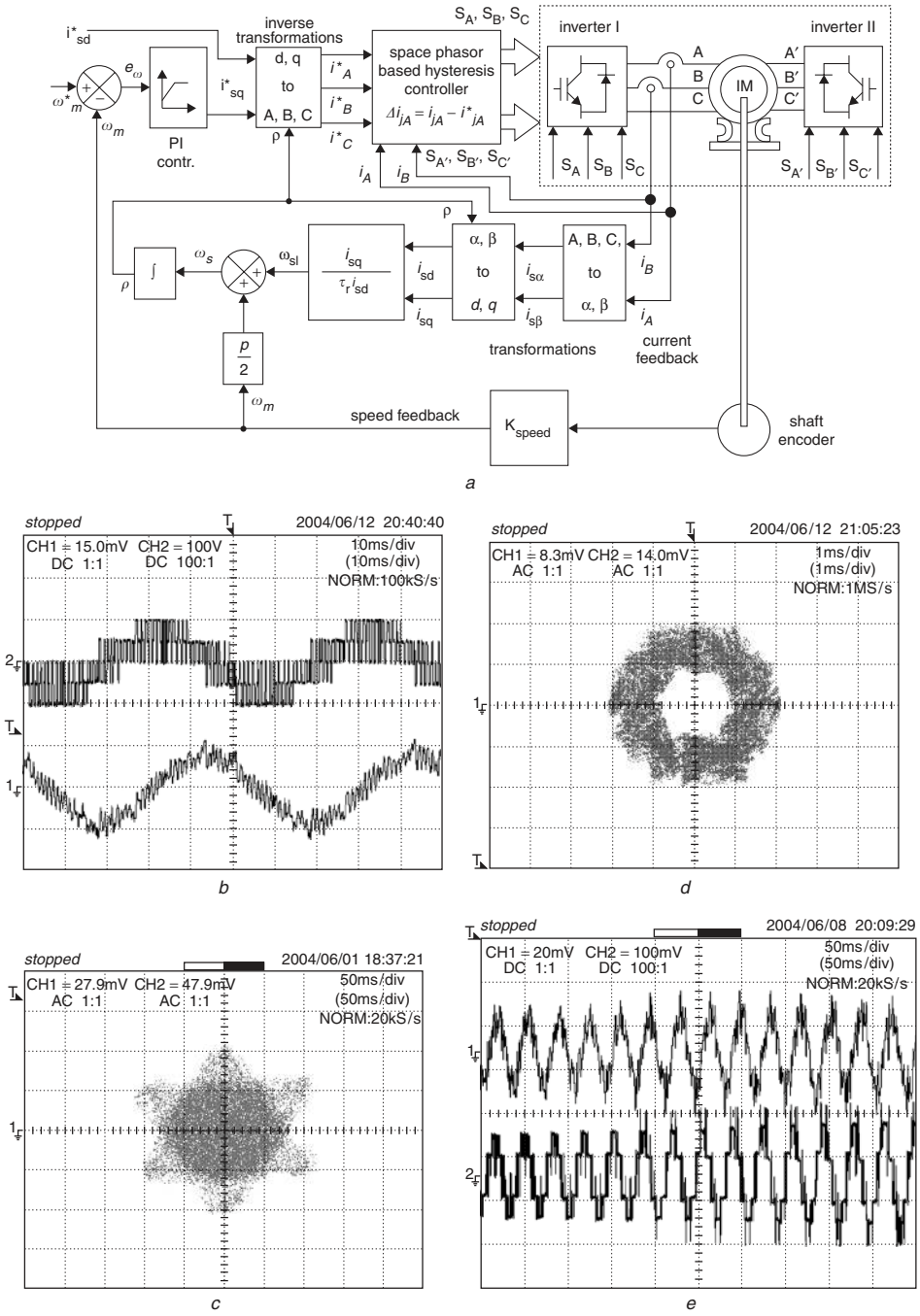

Fig. 5

a Block schematic of proposed hysteresis PWM controller for three-level VSI fed induction motor drive

b Machine phase (AA′) voltage and current (two-level operation, 560 rpm, no load); *y*-axis: voltage (upper trace): 1 div. = 100 V, current (lower trace): 1 div. = 1.5 A; *x*-axis: time: 1 div. = 0.01 s

c Current-error space vector boundary (two-level operation of Fig. 5*b*) [*x*-axis, *y*-axis: 1 div. = 0.3 A]

d Machine current space vector (two-level operation of Fig. 5*b*) [*x*-axis, *y*-axis: 1 div. = 0.75 A]

e Machine phase (AA′) current and voltage (transition from two-level to three-level operation, from 560 to 900 rpm, no load); *y*-axis: current (upper trace): 1 div. = 2 A, voltage (lower trace): 1 div. = 100 V; *x*-axis: time: 1 div. = 0.05 s

f Machine phase (AA′) voltage and current (three-level operation, 950 rpm, no load); *y*-axis: voltage (upper trace): 1 div. = 100 V, current (lower trace): 1 div. = 1.5 A; *x*-axis: time: 1 div. = 0.01 s

g Current-error space vector boundary (three-level operation of Fig. 5*f*) [*x*-xis, *y*-axis: 1 div. = 0.3 A]

h Machine-current space vector (three-level operation of Fig. 5*f* [*x*-axis, *y*-axis: 1 div. = 0.75 A]

i Machine phase (AA′) voltage and current (transition from three-level to two-level operation, 900 to 560 rpm, no load); *y*-axis: voltage (upper trace): 1 div. = 100 V, current (lower trace): 1 div. = 2 A; *x*-axis: time: 1 div. = 0.1 s

j Machine phase (AA′) voltage and current (over-modulation, 1400 rpm, no load); *y*-axis: voltage (upper trace): 1 div. = 100 V, current (lower trace): 1 div. = 2 A; *x*-axis: time: 1 div. = 0.005 s

k Machine current space vector (over-modulation of Fig. 5*j*); [*x*-axis; *y*-axis: 1 div. = 0.75 A]

l Machine current space vector (12-step operation, 1420 rpm, no load) [*x*-axis, *y*-axis: 1 div. = 0.75 A]

m Machine current space vector (980 rpm, with loading) [*x*-axis, *y*-axis: 1 div. = 1.5 A]

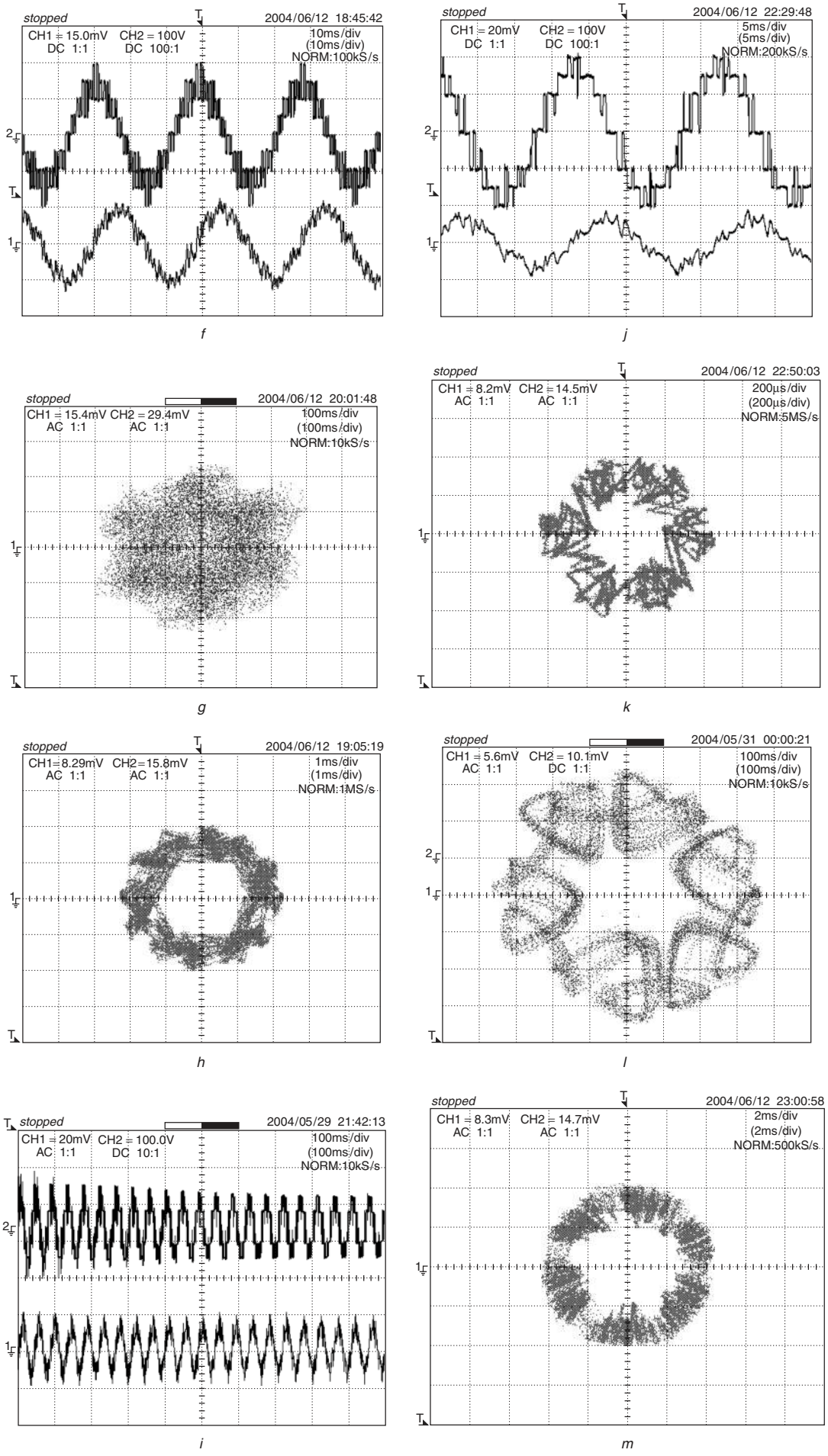

Fig. 5 *Continued*

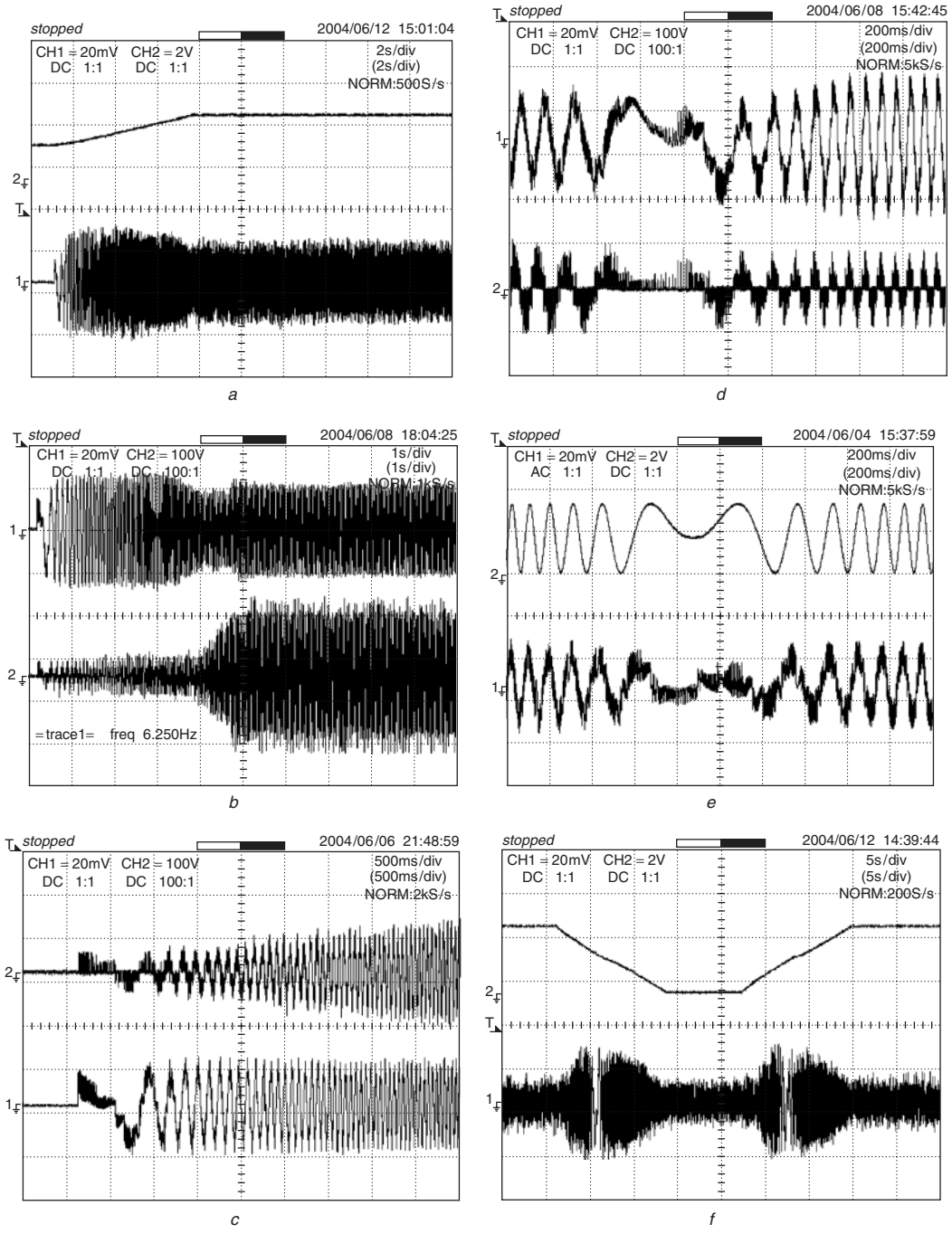

Fig. 6

a Machine speed and phase current (starting of machine from zero speed to 1100 rpm, no load); *y*-axis: speed (upper trace): 1 div. = 1760 rpm, current (lower trace): 1 div. = 2 A; *x*-axis: time: 1 div. = 2 s

b Machine phase (AA′) current and voltage (starting of machine from zero speed to 1100 rpm, no load); *y*-axis: current (upper trace): 1 div. = 2 A, voltage (lower trace): 1 div. = 100 V; *x*-axis: time: 1 div. = 1 s

c Machine phase (AA′) voltage and current (starting of machine, no load); *y*-axis: voltage (upper trace): 1 div. = 100 V, current (lower trace): 1 div. = 2 A; *x*-axis: time: 1 div. = 0.5 s

d Machine phase (AA′) current and voltage (speed reversal of machine, no load); *y*-axis: current (upper trace): 1 div. = 2 A, voltage (lower trace): 1 div. = 100 V; *x*-axis: time: 1 div. = 0.2 s

e Reference and actual machine phase currents (speed reversal of machine, no load); *y*-axis: reference current (upper trace): 1 div. = 2 A, machine current (lower trace): 1 div. = 2 A; *x*-axis: time: 1 div. = 0.2 s

f Machine speed and phase current (speed reversals of machine from 1150 rpm (forward) to 1150 rpm (reverse), no load); *y*-axis: speed (upper trace): 1 div. = 1760 rpm, current (lower trace): 1 div. = 2 A; *x*-axis: time: 1 div. = 5 s

g Normalised harmonic spectrum of phase current of Fig. 5*b* for two-level operation; *y*-axis: normalised amplitude 1 div. = 0.2; *x*-axis: order of harmonic: 1 div. = 10

h Normalised harmonic spectrum of phase current of Fig. 5*f* for three-level operation; *y*-axis: normalised amplitude 1 div. = 0.2; *x*-axis: order of harmonic: 1 div. = 10

i Normalised harmonic spectrum of phase voltage of Fig. 5*b* for two-level operation; *y*-axis: normalised amplitude 1 div. = 0.2; *x*-axis: order of harmonic: 1 div. = 10

j Normalised harmonic spectrum of phase voltage of Fig. 5*f* for three-level operation; *y*-axis: normalised amplitude 1 div. = 0.2; *x*-axis: order of harmonic: 1 div. = 10

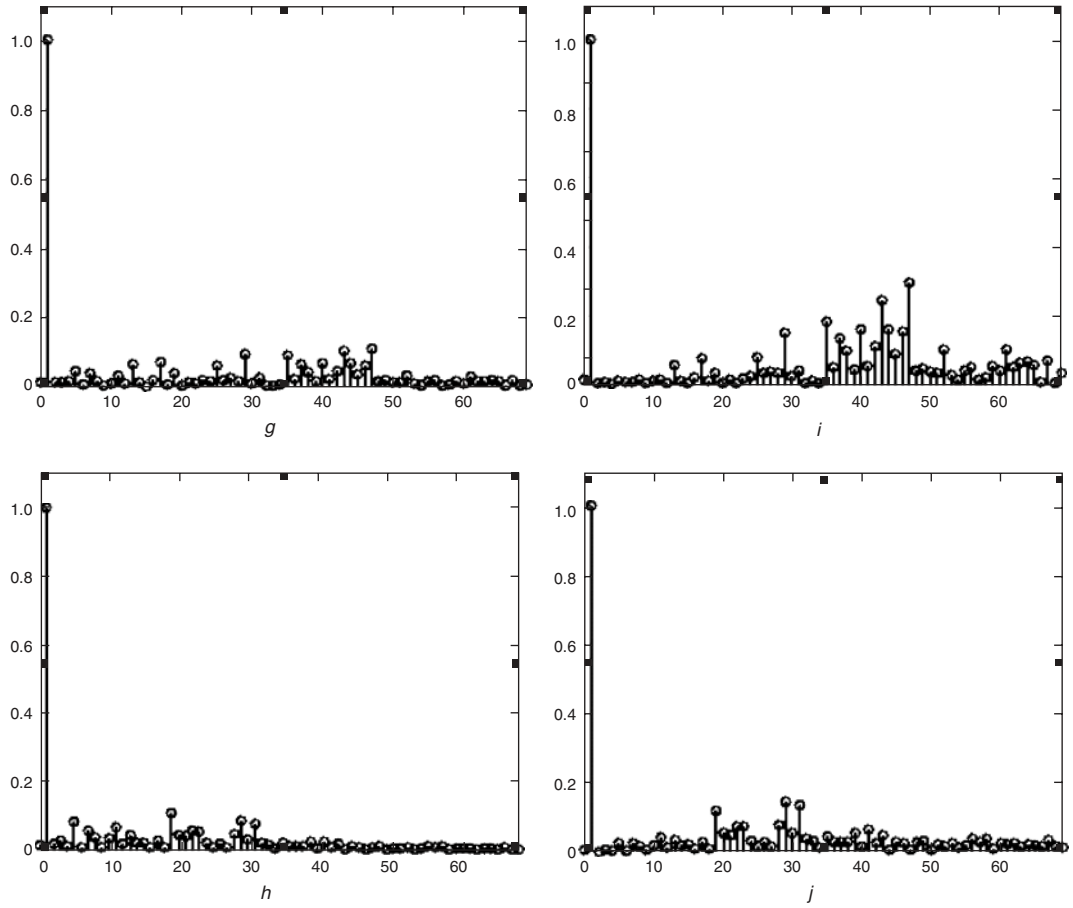

Fig. 6 *Continued*

Experimental results demonstrating the performance of the proposed controller during steady state and transient operations are shown in Figs. 5*b* to 6*j*, where Fig. 5*b* shows the machine phase voltage and current for lower speed command in the linear range. In the steady-state results, no-load motor phase current waveforms are presented, so that the current ripple can be clearly seen. The phase voltage profile indicates that the inverter is operating in two-level mode of operation and adjacent vectors are always selected conforming to optimum PWM switching. The phase current profile remains smooth even during sector change. Figure 5*c* shows that the current-error space vector is kept within the hexagonal boundary all the time, except during the sector change, where it briefly crosses the boundary in two-level operation. Figure 5*d* shows the machine current space vector, indicating a rotating space vector profile. A smooth transition from two-level to three-level operation of inverter is shown in Fig. 5*e*, showing the transient performance of the drive. Similar results are obtained for the higher speed operations of drive in the linear range. Figure 5*f* shows the phase voltage and current during three-level operation, and the current-error space vector and the machine current space vector are shown in Figs. 5*g* and *h*, respectively. Smooth transition from three-level to two-level operation of the inverter is shown in Fig. 5*i*, which indicates the self-adaptiveness of the controller. Figure 5*j* shows the machine voltage and current for further higher-speed operation, where the drive is running in the over-modulation region. It can be seen from the presented voltage waveforms for different speeds that the proposed controller logic is capable of retaining the feature of adjacent voltage vector switching throughout the operating range of the drive. The machine current space vector for the same over-modulation operation is shown in Fig. 5*k*. Figure 5*l* shows the machine current space vector when the inverter is operating in 12-step mode of operation. Figure 5*m* shows the machine current space vector, when the motor is loaded, and it shows a circular profile for the actual machine current space vector.

Starting current profile of machine with the speed of the machine is shown in Fig. 6*a* presenting smooth starting current of the machine. Figure 6*b* shows the starting current profile of machine with machine phase voltage. An expanded view (on timescale) of the machine phase voltage and phase current waveforms for starting operation is shown in Fig. 6*c*. The performance of the controller during speed reversal is presented by machine phase current and voltage waveforms, as shown in Fig. 6*d*. Tracking of machine phase current with reference phase current during the speed reversal operation is shown in Fig. 6*e*. It shows that the machine phase current remains within the set control band and always tracks the reference phase current. Figure 6*f* shows machine speed and machine phase current profile for two consecutive speed reversal commands. The normalised harmonic spectra of machine phase current during two-level (shown in Fig. 5*b*) and three-level (shown in Fig. 5*f*) operation of inverter are shown in Figs. 6*g* and *h*, respectively. The spectra show the absence of subharmonics in the current waveforms. Figures 6*i* and *j* show the normalised harmonic spectra of machine phase voltages for two-level (shown in Fig. 5*b*) and three-level (shown in Fig. 5*f*) operation, respectively, showing the absence of lower-order harmonics in the machine phase voltages. The spread spectra of harmonics shown in Figs. 6*g–j* are as expected. Because of the adjacent voltage vector switching, the large magnitude harmonics at frequencies lower than

the fundamental (subharmonics, present in conventional hysteresis controller) are absent in the proposed scheme.

5 Conclusions

A current-error space-vector-based hysteresis PWM controller is presented for three-level voltage source inverter fed drive applications. A hexagonal boundary for current-error space vector is formed by monitoring the current errors along the j_A, j_B and j_C axes. Computation of the machine back EMF vector is not needed and information of the same is derived indirectly from the direction of the current-error space vector. Region detection and sector detection are achieved by simple logic. Selection of the appropriate inverter voltage vector is done by using a simple look-up table. Among the three adjacent vectors forming a triangular sector, in which the tip of the machine voltage vector lies, the inverter voltage vector, which results in the largest current error deviation in the opposite direction, is selected throughout the operating range. This ensures the optimum PWM switching and fast dynamic response of the controller. The controller is capable of operating the machine in two-level, three-level and over-modulation ranges up to 12-step mode of operation, with smooth transition from one to another level and vice versa. The scheme is thus self-adaptive for any possible amplitude and position of machine voltage vector. High-frequency hexagonal switching is eliminated by properly identifying the boundary regions for the inverter vector selection. Sector inhibition logic prevents false sector change detection and helps the controller to switch the most appropriate voltage vectors of the inverter. Alternative clamping of individual inverter on the same switching state ensures equal switching in both two-level inverters over a fundamental period of reference current. All the advantages of conventional hysteresis controllers, e.g. quick dynamic response and simple implementation, are retained in the proposed scheme with the added advantage of space vector modulation. The scheme can be applied to any inverter configuration that generates three-level voltage space vector structure. Experimental verification of the proposed scheme is achieved on a dual two-level VSI fed open-end winding induction motor drive. The performance of the controller has been demonstrated by experimental results of steady state and transient conditions of drive. The proposed scheme can be easily extended to multilevel operations for high-performance drive applications by constructing proper look-up tables.

6 References

1 Kazmierkoswki, M.P., and Malesani, L.: 'Current control techniques for three phase voltage source PWM converters: a survey', *IEEE Trans. Ind. Electron.*, 1998, **45**, (5), pp. 691–703

2 Nagy, I.: 'Novel adaptive tolerance band based PWM for field-oriented control of induction machines', *IEEE Trans. Ind. Electron.*, 1994, **41**, (4), pp. 406–417

3 Brod, D.M., and Novotny, D.W.: 'Current control of VSI-PWM inverters', *IEEE Trans. Ind. Appl.*, 1985, **IA-21**, (4), pp. 562–570

4 Salama, S., and Lennon, S.: 'Overshoot and limit cycle free current control method for PWM inverters'. Proc. European Conf. on Power Electronic Applications (EPE), Firenze, Italy, 1991, pp. 3/247–251

5 Kwon, B.H., Kim, T.W., and Youm, J.H.: 'Novel SVM-based hysteresis current controller', *IEEE Trans. Power. Electron.*, 1998, **13**, (2), pp. 297–307

6 Nagy, I., Suto, Z., and Backhausz, L.: 'Periodic states of hysteresis current control of induction motor'. Proc. 29th European Conf. on Intelligent Motion (PCIM), Nurnberg, Germany, May 1996, pp. 605–619

7 Nabae, A., Ogasawara, S., and Akagi, H.: 'A novel control scheme for current controlled PWM inverters', *IEEE Trans. Ind. Appl.*, 1986, **IA-22**, (4), pp. 697–701

8 Mistry, V.M., Waikar, S.P., Gopakumar, K., Umanand, L., and Ranganathan, V.T.: 'A multi axis space phasor based current hysteresis controller for PWM Inverters', *EPE J.*, 2000, **10**, (1), pp. 17–25

9 Baiju, M.R., Gopakumar, K., Umanand, L., and Pittet, A.: 'Multi axis space phasor based multi level current hysteresis controller for an open-end winding induction motor fed from dual inverters'. Proc. 29th European Conf. on Intelligent Motion (PCIM), Nurnberg, Germany, 2002, pp. 405–410

10 McMurray, W.: 'Modulation of the chopping frequency in DC choppers and PWM inverters having current-hysteresis controllers'. Proc. PESC, 1983, pp. 3/295–299

11 Wuest, D., and Jenni, F.: 'Space vector based current control schemes for voltage source inverters'. Proc. Power Electronics Specialists Conf. (PESC). 1993, June 1993, pp. 986–992

12 Kazmierkoswki, M.P., Dzieniakowski, M.A., and Sulkowski, W.: 'Novel space vector based current controllers for PWM-inverters', *IEEE Trans. Power Electron.*, 1991, **6**, (1), pp. 158–166

13 Ackva, A., Reinold, H., and Olenski, R.: 'A simple and self-adapting high-performance current control scheme for three phase voltage source inverters'. Proc. IEEE IAS Conf., 1992, pp. 435–442

14 Nagy, I., and Backhausz, L.: 'Current control of VSI-PWM inverters for vector controlled drives'. Proc. 25th European Conf. on Intelligent Motion (PCIM), Nurnberg, Germany, June 1994, pp. 397–413

15 Baiju, M.R., Mohapatra, K.K., Kanchan, R.S., Tekwani, P.N., and Gopakumar, K.: 'A space phasor based self adaptive current hysteresis controller using adjacent inverter voltage vectors with smooth transition to six step operation for a three phase voltage source inverter', *EPE J.*, 2005, **15**, (1), pp. 36–47

16 Bode, G.H., Zmood, D.N., Loh, P.C., and Holmes, D.G.: 'A novel hysteresis current controller for multilevel single phase voltage source inverters'. Proc. IEEE Power Electronics Specialists Conf. (PESC), 2001, pp. 1845–1850

17 Loh, P.C., Bode, G.H., Holmes, D.G., and Lipo, T.A.: 'A time-based double band hysteresis current regulation strategy for single-phase multilevel inverters'. Proc. IEEE-IAS Annual Meeting, 2002, pp. 1994–2001

18 Corzine, K.A.: 'A hysteresis current–regulated control for multi-level drives', *IEEE Trans. Energy Convers.*, 2000, **15**, (2), pp. 169–175

19 Stemmler, H., and Guggenbach, P.: 'Configurations of high power voltage source inverter drives'. Proc. European Conf. Power Electronic Applications (EPE), Brighton, UK, 1993, pp. 7–12

20 Shivakumar, E.G., Gopakumar, K., Sinha, S.K., Pittet, A., and Rangnathan, V.T.: 'Space vector PWM control of dual inverter fed open-end winding induction motor drive', *EPE J.*, 2002, **12**, (1), pp. 9–18

21 Baiju, M.R., Mohapatra, K.K., Kanchan, R.S., and Gopakumar, K.: 'A dual two-level inverter scheme with common mode voltage elimination for an induction motor drive', *IEEE Trans. Power Electron.*, 2004, **19**, (3), pp. 794–805